Electronic Supplementary Material (ESI) for RSC Advances.

A New Ru (II) Polypyridyl Complex as an Efficient Photosensitizer for Enhancing the Visible-Light-Driven photocatalytic activity of TiO_2/Reduced Graphene Oxide Nanocomposite for the Degradation of Atrazine; DFT and Mechanism Insights

Amir Hossein Cheshme Khavar[1], Gholamreza Moussavi[2*], Ali Reza Mahjoub[3*], Neda Khedri[3], Michal Dusek[4], Tereza Vaclavu[4], Mahdieh Hosseini[3]

1. Department of Chemistry, Faculty of Basic Sciences, Shahid Bahonar Campus, Farhangian University, Isfahan, Iran
2. Department of Environmental Health Engineering, Faculty of Medical Sciences, Tarbiat Modares University, Tehran, Iran
3. Department of Chemistry, Faculty of Basic Sciences, Tarbiat Modares University, Tehran, Iran
4. Institute of Physics ASCR, Na Slovance 2, 182 21 Prague, Czech Republic

1. Synthesis of GO

Briefly, 1.0 g graphite was added into 46 mL sulfuric acid (97%) and stirred for 20 min in an ice bath. Then 1.0 g NaNO3 was added and the mixture was stirred for 1 h. 6.0 g KMnO4 was then gradually added to the mixture at 0 °C. The mixture was subsequently heated to 40 °C for 1 h. 80 mL DW was then injected into the mixture, which led to increasing the solution temperature up to 90 °C. The temperature was maintained at 90 °C for 30 min. Additional 100 mL DW was then added into the mixture. This was followed by the slow addition of 10 mL of H2O2 (30%). The warm solution was filtered using a filtration system under vacuum condition and the filtrate was added to 100 mL DW, followed by sonication for 10 min. The pellet was then washed several times with DW until a neutral pH was obtained.

2. Synthesis of TiO_2 nanoparticles

Briefly, 10 mL DW was added dropwise with the rate of 1 mL/min into 25 mL titanium isopropoxide (TTIP) 1.3 mol/L solution in isopropanol in an ultrasonic bath. The resulted suspension was stirred using magnetic stirring for 2 h to form a homogenous gel. The final gel was dried in an oven at 60 °C overnight. The prepared powder was calcined at 500 ˚C (at 1 °C/min) for 2 h in a muffle furnace under N_2 atmosphere.

3. Analytical methods and performance indices

The concentration of ATZ was analyzed by a high-performance liquid chromatography (HPLC, Eclipse Plus C18column; 3.5 µm, 4.6 × 100 mm, Agilent Co.) with a UV detector at 203 nm. The mobile phase was a mixture of phosphate buffer (pH = 4.8) and acetonitrile at 85:15 (v/v%) injected at the flow rate of 1.0 mL/min. The degradation of ATZ was calculated from Eq. (1).

$$Removal\ efficiency\ (\%) = \frac{ATZ_0 - ATZ_t}{ATZ_0} \times 100 \quad (1)$$

where ATZ_0 and ATZ_t demonstrate the ATZ concentrations at the beginning and time t of the reaction, respectively.

The degree of ATZ mineralization was determined under optimum experimental conditions based on TOC measurements from Eq. (2).

$$Mineralization\ (\%) = \frac{TOC_0 - TOC_t}{TOC_0} \times 100 \quad (2)$$

where TOC_0 and TOC_t demonstrate the ATZ concentrations at the beginning and time t of the reaction, respectively. The concentration of TOC was measured using a TOC analyzer (Shimadzu, TOC analyzer -VCSH model).

The kinetics of ATZ degradation/mineralization was evaluated with the pseudo-first order (PFO) reaction model (Eq. (3)).

$$ln\left(\frac{C_t}{C_0}\right) = -k_{obs}t \quad (3)$$

The observed PFO rate of ATZ degradation (r_{obs}, mg/L.min) was calculated from Eq. (4).

$$r_{obs} = -k_{obs}C_0 \quad (4)$$

C_t and C_0 are the ATZ concentration (mg/L) at the beginning and time t (min) of the reaction. The observed PFO reaction constant (k_{obs}) and rate (r_{obs}) of ATZ degradation/mineralization was determined by fitting Eq. (3) and Eq. (4), respectively, to the experimental results shown in.

Table S1 Crystal data and structural refinement parameters for complex **[Ru(tptz)(ACN)Cl_2].**

Compound	**[Ru(tptz)(ACN)Cl_2]**
formula	$C_{20}H_{15}Cl_2N_7Ru$
f_w	525.36
λ/Å	1.54184
T/K	95
crystal system	Triclinic
space group	Pī
a/Å	9.2254(16)
b/Å	10.6015(18)
c/Å	12.161(2)
α/°	87.997(14)
β/°	71.097(16)
γ/°	87.572(14)
V/Å^3	1123.9(3)
D_{calc}/Mg m^{-3}	1.552
Z	2
μ/mm^{-1}	8.008
F(000)	524
2θ/°	153.2
R(int)	0.079
GOOF	2.46
R_1 ($I > 2\sigma(I)$)	0.1505
wR_2 ($I > 2\sigma(I)$)	0.1980
CCDC No.	1923285

Table S2 Selected bond length (Å) and angles (°) around ruthenium for complexes **[Ru(tptz)(ACN)Cl_2].**

Ru1–Cl1	2.379(6) Å	Ru1–Cl2	2.398(7)Å
Ru1–N1	1.923(18) Å	Ru1–N4	2.05(2) Å
Ru1–N6	2.033(19) Å	Ru1–N7	2.062(18) Å
Cl1–Ru1–Cl2	176.6(2)°	Cl1–Ru1–N1	90.8(6)°
Cl1–Ru1–N4	88.4(6)°	Cl1–Ru1–N6	90.2(6)°
Cl1–Ru1–N4	131.12(18)°	Cl1–Ru1–N7	89.2(5)°
Cl2–Ru1–N1	92.6(6)°	Cl2–Ru1–N4	88.3(6)°
Cl2–Ru1–N6	90.4(6)°	Cl2–Ru1–N7	91.4(5)°
N1–Ru1–N4	178.1(8)°	N1–Ru1–N6	81.0(8)°
N1–Ru1–N7	78.3(7)°	N4–Ru1–N6	97.2(8)°
N4–Ru1–N7	103.4(8)°	N6–Ru1–N7	159.3(7)°

Table S3 Hydrogen bond geometries for **[Ru(tptz)(ACN)Cl_2].**

D–H Error!**A**	***d*(D–H)/ Å**	***d*(H**Error!**A)/ Å**	***d*(D**Error!**A)/ Å**	**∠(D–H**Error!**A)/°**	**Symmetry**
		I			
C5–H2c5···Cl2	0.96	2.83	3.65(3)	143	1–x, 1–y, 1–z
C17–H1c17···Cl1	0.96	2.80	3.54(2)	134	1–x, 1–y, –z
C12–H1c12···Cl2	0.97	2.95	3.59(3)	125	–x,–y, 1–z
C14–H1c14···Cl1	0.96	2.81	3.60(2)	140	–x , 1–y, 1–z

Table S4 π–interaction geometries for **[Ru(tptz)(ACN)Cl_2].**

Structure	**Interaction**	**D**Error!**A**	**C-C (Å)**	**P-P°**	**P-CC°**	**C**Error! **Cg (Å)**	**C-H-Cg /°**	**Symm. code**
C_1	π_{py}–π_{py}	Cg6**Error!**Cg6	3.764(12)	0.00	31.52	---	---	1–x, 1–y,–z
	π_{py}–$\pi_{s\text{-}triazine}$	Cg3**Error!**Cg4	3.694(16)	6.10	24.24, 25.32	---	---	–x,–y,–z
	π_{py}–π_{py}	Cg6**Error!**Cg4	3.631(16)	3.27	24.34, 27.33	---	---	1–x,–y,–z
	CH**Error!**$\pi_{s\text{-}triazine}$	C12–H1c12**Error!**Cg3				3.78	93	–x,–y,1–z
	CH**Error!**π_{py}	C5–	---	---	---	3.62	141	–x, 1–y, 1–z

H3c5**Error!**Cg5

Cg stands for the center of gravity of the mentioned ring:
Cg3: N1–N3, C1–C3; **Cg4**: N5, C6–C10; **Cg5:** N6, C11–C15; **Cg6:** N7, C16–C20.

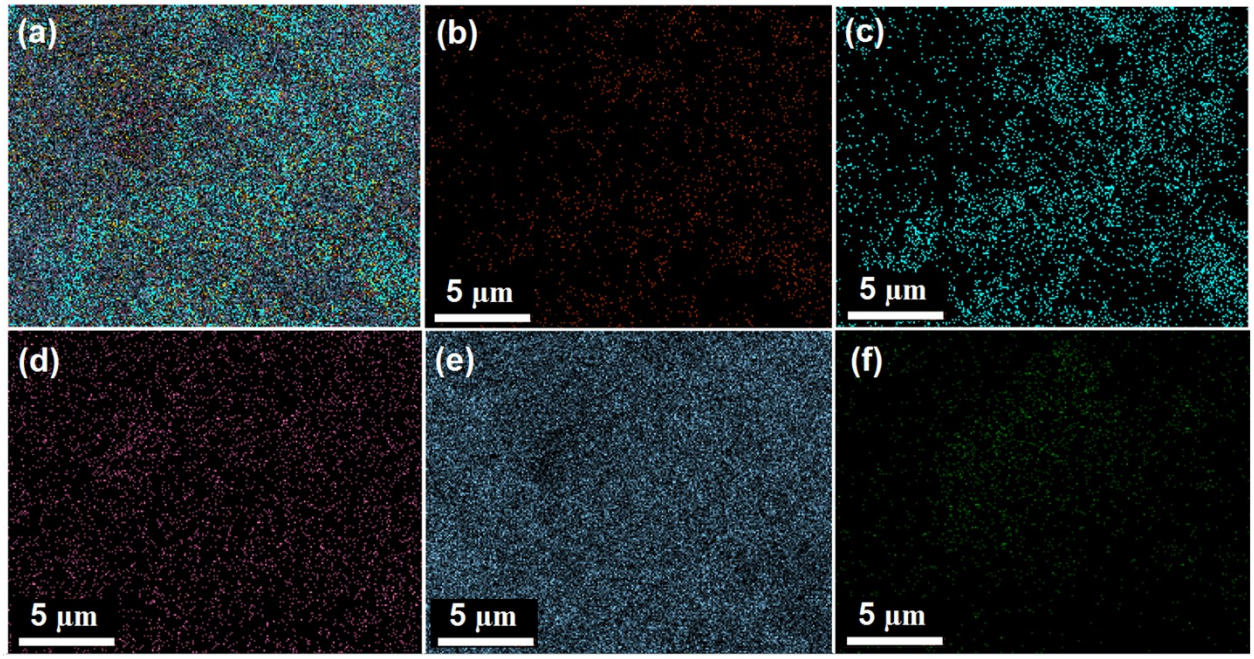

Figure S1: The elemental mapping of (a) Ru-CMP-TiO_2/rGO sample, (b) carbon, (c) chlorine, (d) ruthenium (e) titanium and (f) nitrogen. The elemental mapping of Ru-CMP-TiO_2/rGO for titanium, ruthenium, carbon, nitrogen and is observed in Figure S1, which confirms the presence of these elements with uniform distribution in the sample.

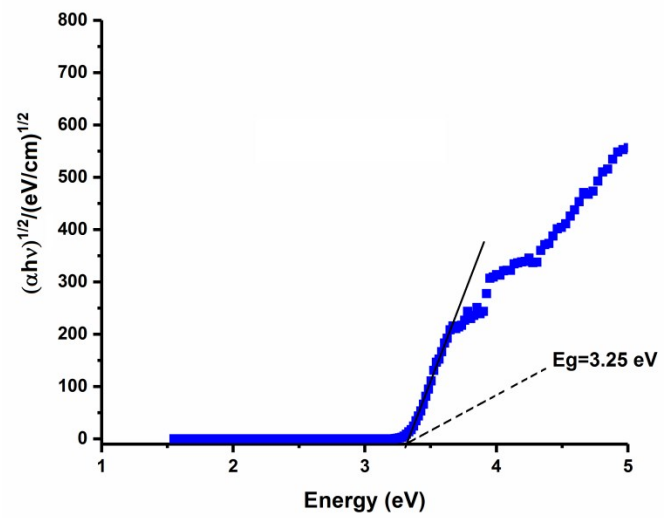

Figure S2. Tuce plots for determining the band gap energy of TiO_2.

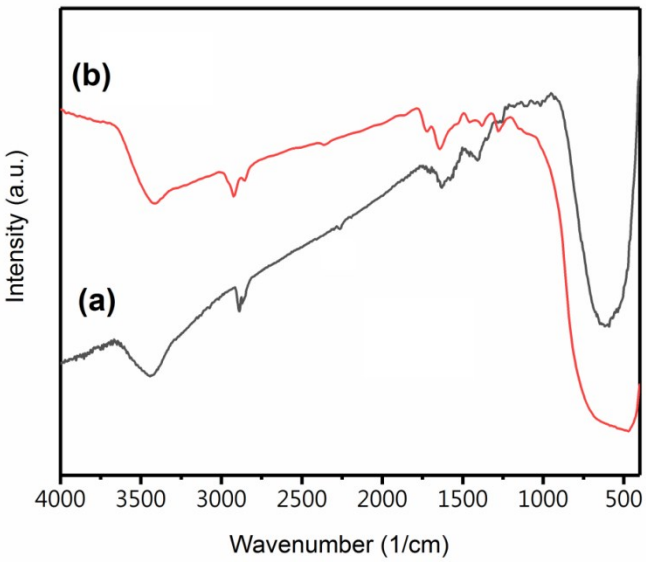

Figure S3: FT-IR spectra of Ru-CMP-TiO_2/rGO sample before (a) and after (b) photocatalytic reaction. As can be seen, any remarkable change is seen in the FT-IR of catalyst after photocatalytic reaction and the resulted FT-IR are completely matched with the FT-IR peaks of sample before photocatalytic reaction and no systematic peak position shift was detected after photocatalytic reaction 60 min.

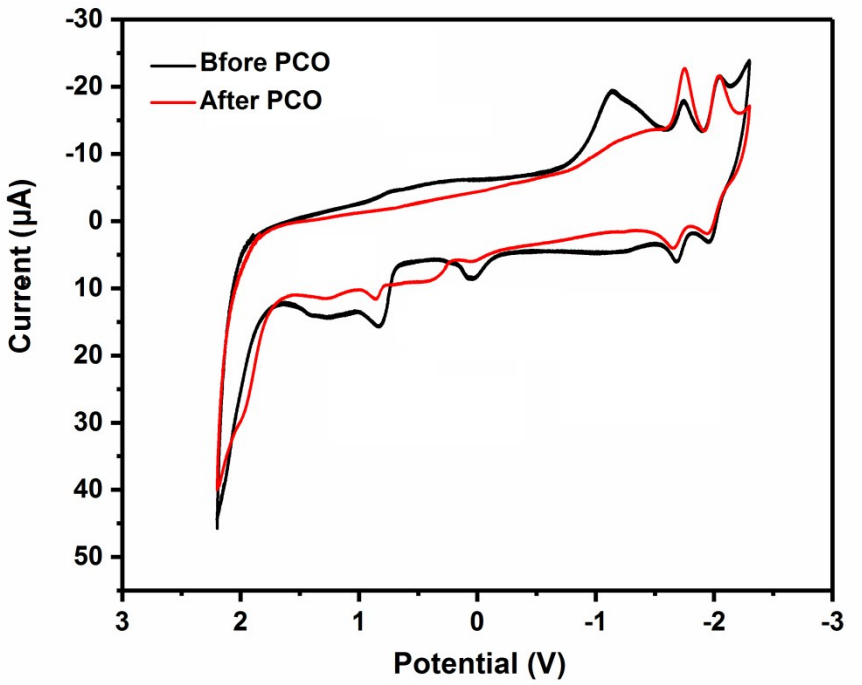

Figure S4: Cyclic voltammograms of Ru-CMP-TiO_2/rGO hybrid before and after photocatalytic reaction. Similar redox behavior was achieved for the Ru-CMP-TiO_2/rGO hybrid after photoctacalytic oxidation process and into TiO_2/rGO nanocomposite without detectable peak position shift.

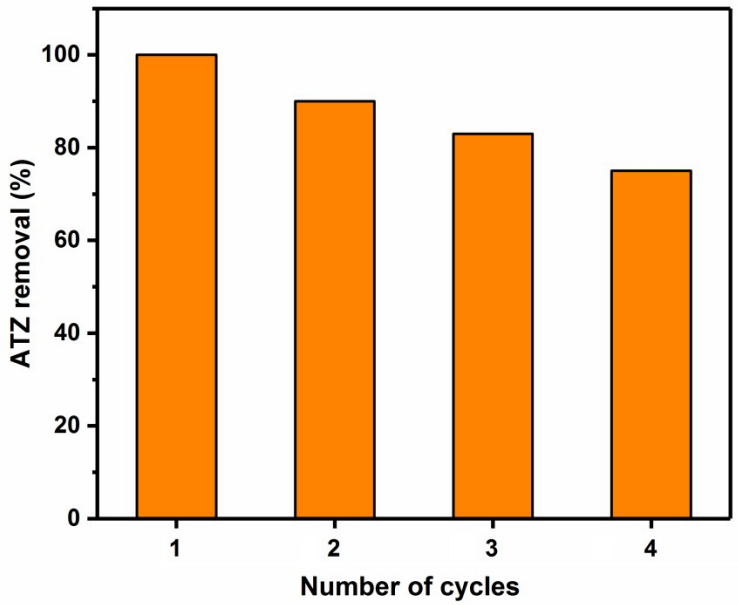

Figure S5: The stability and durability of the synthesized photocatalyst in the photocatalytic degradation of atrazine. The reusability of the prepared catalyst was studied under experimental conditions pH=5.4, ATZ concentration=20 mg/L and reaction time=60 min. The reusability tests were repeated for 4 consecutive times under the same experimental conditions using the catalyst reused from the previous test. The photocatalytic activity were kept at high after three consecutive times reuse. The deactivation is because of the inevitable loss of catalyst during the recovery process.